crystals

MDPI

Corrosion Behavior of $Cr_{19}Fe_{22}Co_{21}Ni_{25}Mo_{13}$ Alloy in 1M Nitric Acid and 1M Hydrochloric Acid Solutions

Chun-Huei Tsau * and Po-Min Chen

Institute of Nanomaterials, Chinese Culture University, Taipei 111, Taiwan; stevenchen8900@gmail.com
* Correspondence: chtsau@staff.pccu.edu.tw

Abstract: The present work studied the microstructures of $Cr_{19}Fe_{22}Co_{21}Ni_{25}Mo_{13}$ alloy, and tested the polarization properties in deaerated 1M nitric acid and 1M hydrochloric solutions at different temperatures. The alloy was processed by an argon atmosphere arc-melting. Results indicated that the microstructure of $Cr_{19}Fe_{22}Co_{21}Ni_{25}Mo_{13}$ alloy was a dendritic one. The dendrites of $Cr_{19}Fe_{22}Co_{21}Ni_{25}Mo_{13}$ alloy were an FCC structure, and the interdendrites of $Cr_{19}Fe_{22}Co_{21}Ni_{25}Mo_{13}$ alloy were a eutectic structure with two phases of FCC and simple cubic (SC). The $Cr_{19}Fe_{22}Co_{21}Ni_{25}Mo_{13}$ alloy had better corrosion resistance compared with commercial 304 stainless steel in both deaerated 1M HNO_3 and 1M HCl solutions. The corrosion types of $Cr_{19}Fe_{22}Co_{21}Ni_{25}Mo_{13}$ alloy in both of 1M HNO_3 and 1M HCl solutions were uniform corrosion.

Keywords: $Cr_{19}Fe_{22}Co_{21}Ni_{25}Mo_{13}$; microstructure; corrosion; polarization

1. Introduction

Iron, chromium, nickel, and cobalt are the main elements of stainless steels; many corrosion-resistant alloys are developed based on these elements. The CoCrFeNiSn had a good passivation in chloride solution because the surface had stable oxide films [1]. The study of corrosion behaviors of $Al_xCrFeCoNi$ high-entropy alloys showed that the corrosion resistance increased by decreasing aluminum content and increasing chromium content in 3.5% NaCl solution [2]. The corrosion study of $(CoCrFeNi)_{100-x}Mo_x$ alloys indicated that the addition of molybdenum could increase the corrosion resistance in 3.5% NaCl solution, and these alloys would form the passivation films to improve corrosion resistance in 0.5M H_2SO_4 solution [3]. $Al_{0.5}CoCrCuFeNi$ high-entropy alloy was coated on the surface of AZ91D magnesium alloy by laser cladding to improve the corrosion resistance, and results showed the corrosion potential increased, and the corrosion current density decreased [4]. The non-equiatomic CrFeCoNiMo high-entropy alloy was irradiated by electron beam to modify the surface, and the electrochemical results indicated that the alloy had a positive potential and lower current density in 3.5 wt.% NaCl solution [5]. Only 0.1 mol addition of Zr into $AlCoCrFeNiZr_x$ alloys could greatly improve the corrosion resistance of the alloys in 0.5 M H_2SO_4 solution [6]. The $Al_{0.1}CoCrFeNi$ high-entropy alloy had higher polarization resistance and lower corrosion rate compared with nickel-based Alloy 718 in a molten Na_2SO_4-NaCl eutectic mixture at 750 ± 5 °C [7]. The CoCrFeNi (WC) coatings WC was 10–30 wt.%, and all enhanced corrosion resistance in 3.5% NaCl solution. Particularly, the added 10 wt.% WC clearly enhanced the comprehensive corrosion resistance and easy passivation of the alloy [8]. Our previous studies showed that the CrFeCoNi(Nb,Mo) alloys [9] and $CrFeCoNiNb_x$ alloys [10] all had better corrosion resistance than commercial 304 stainless steel. These alloys indicated that the CrFeCoNi-based alloys had a potential to develop alloys with good corrosion resistance. The alloys described above are all high-entropy alloys. The researchers can develop new alloys based on the high-entropy alloy concept and smartly choose the suitable elements to develop the alloys for the applications [11,12].

The CrFeCoNiMo high-entropy alloy [9] had a dual-phased dendritic structure; one was FCC phase with a lattice constant of 3.577 Å, and the other was a simple cubic (SC) phase with a lattice constant of 8.398 Å. Addition of molybdenum into CrFeCoNi alloy would reduce the corrosion resistance of the alloy but significantly increase the hardness of CrFeCoNi alloy. The present work selected the compositions of the FCC phase in CrFeCoNiMo alloy to be a new alloy, $Cr_{19}Fe_{22}Co_{21}Ni_{25}Mo_{13}$, and studied the microstructure and polarization behaviors of this alloy in deaerated 1M nitric acid and 1M hydrochloric acid solutions.

2. Materials and Methods

The nominal chemical compositions of experimental alloy, $Cr_{19}Fe_{22}Co_{21}Ni_{25}Mo_{13}$, was 16.0% of Cr, 19.9% of Fe, 20.1% of Co, 23.8% of Ni, and 20.2% of Mo in weight percent. The alloy was made by an arc furnace in an argon atmosphere after accurately weighing. The total weight of the melt was about 100 g. Following this, the work of microstructure observing and polarization tests was done on the as-cast $Cr_{19}Fe_{22}Co_{21}Ni_{25}Mo_{13}$ alloy. The microstructure of $Cr_{19}Fe_{22}Co_{21}Ni_{25}Mo_{13}$ alloy was observed by a scanning electron microscope (SEM, JEOL JSM-6335, JEOL Ltd., Tokyo, Japan) operated at 10 kV after regular metallurgical processes; the chemical compositions of the phases were measured by energy dispersive spectrometer (EDS). The phases in the alloy were identified by an x-ray diffractometer (XRD, Rigaku ME510-FM2, Rigaku, Tokyo, Japan) with a scanning rate of 0.04 degree per second. The Vicker's hardness of the alloy was tested by Matsuzawa Seiki MV1. The loading force for testing the overall hardness of the alloy was 19.61 N (2000 gf), and the loading force for testing dendrites and interdendrites was 0.245 N (25 gf). The potentiodynamic polarization curves of $Cr_{19}Fe_{22}Co_{21}Ni_{25}Mo_{13}$ alloy were tested by an electrochemical device (Autolab PGSTAT302N, Metrohm Autolab B.V., Utrecht, The Netherlands), with three electrodes at different temperatures of 30, 40, 50, and 60 °C, respectively. One electrode was the specimens, which was mounted in epoxy resin with an exposed area of 0.196 cm^2 (0.5 cm in diameter). The second electrode was a platinum wire used as a counter. The other electrode was a saturated silver chloride electrode (Ag/AgCl, SSE) used as a reference one, and this reference electrode had a potential was 0.197 V higher than the standard hydrogen electrode (SHE) at 25 °C [13]. The polarization test was started after setup for 900 s, and the scanning rate was 1 mV per second. Nitrogen bubble was used to degas the oxygen in the solutions through the process. Two test solutions were 1M nitric acid and 1M hydrochloric acid solutions, which were prepared from reagent-grade acids and deionized water.

3. Results and Discussion

The SEM micrograph and XRD pattern of as-cast $Cr_{19}Fe_{22}Co_{21}Ni_{25}Mo_{13}$ alloy are shown in Figure 1a,b, respectively. Figure 1a is the micrograph that shows a typical dendritic microstructure. The dendrites had a face-centered cubic (FCC) phase, and the interdendritic regions were a eutectic structure with FCC and simple cubic (SC) phases. The micrograph displays that the volume fraction of FCC phase is more than that of SC phase. The chemical compositions of the overall, FCC, and SC phases are listed in Table 1. The overall compositions of $Cr_{19}Fe_{22}Co_{21}Ni_{25}Mo_{13}$ alloy indicates that actual compositions of this alloy almost match the origin design. Additionally, the Fe, Co, and Ni content of FCC phase are more than those of SC phase; but the Cr and Mo content of FCC phase are less than those of SC phase. The SC phase is brighter than the FCC phase in the SEM micrograph because SC phase has more Mo content, which atomic number is higher than the other four elements. This is the backscattering effect of the electrons in SEM observing. Figure 1b is the XRD pattern of as-cast $Cr_{19}Fe_{22}Co_{21}Ni_{25}Mo_{13}$ alloy, and it shows only two phases, FCC and SC, in this alloy. The lattice constants of FCC and SC phases are 3.611 and 8.320 Å, respectively. The structure of SC phase has been identified in our previous work [9]; the large lattice constant of SC phase indicates that the unit cell of SC phase has many atoms and a complex structure. The XRD pattern also proves that the FCC

phase is more than SC phase by comparing the intensities of the peaks of FCC and SC phases. The hardness of dendrites was 281 ± 11 HV because of the FCC structure. The hardness of interdendrites was 414 ± 12 HV because of the eutectic structure of FCC and HCP phases. The overall hardness of the $Cr_{19}Fe_{22}Co_{21}Ni_{25}Mo_{13}$ alloy was 290 ± 5 HV. The overall hardness of $Cr_{19}Fe_{22}Co_{21}Ni_{25}Mo_{13}$ alloy was only slightly higher than that of FCC-dendrites because the FCC phase was the major phase in this alloy. Therefore, the overall hardness of the alloy was dominated by the FCC-dendrites.
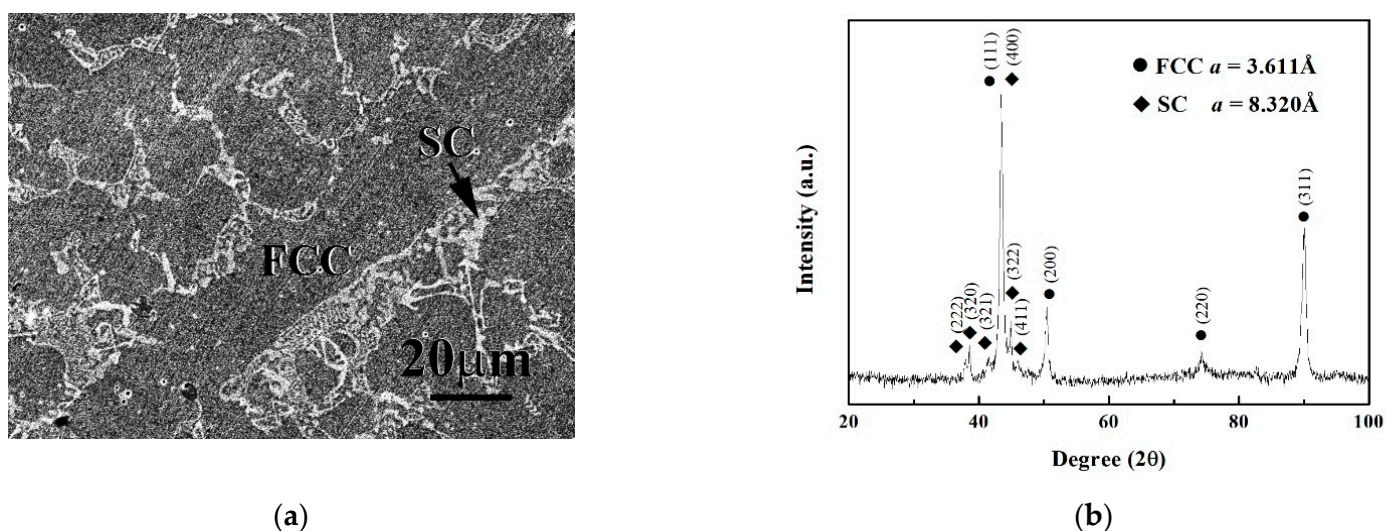

| (a) | (b) |

Figure 1. (a) A micrograph and (b) XRD pattern of as-cast $Cr_{19}Fe_{22}Co_{21}Ni_{25}Mo_{13}$ alloy.

Table 1. Chemical compositions of as-cast $Cr_{19}Fe_{22}Co_{21}Ni_{25}Mo_{13}$ alloy in atomic percent analyzed by SEM/EDS.

Phase	Cr	Fe	Co	Ni	Mo
Overall	18.8 ± 0.6	22.0 ± 0.9	21.2 ± 2.5	24.8 ± 1.2	14.2 ± 0.6
FCC	18.2 ± 0.7	23.2 ± 1.0	20.8 ± 1.3	26.1 ± 0.8	11.7 ± 0.6
SC	20.6 ± 0.8	18.1 ± 1.2	17.8 ± 1.6	16.9 ± 1.9	26.6 ± 2.8

The potentiodynamic polarization curves of $Cr_{19}Fe_{22}Co_{21}Ni_{25}Mo_{13}$ alloy in deaerated 1M HNO_3 and 1M HCl solutions under different temperatures are shown in Figure 2a,b, respectively. The corrosion potential (E_{corr}) is the mixed potential, which means the rate of anodic dissolution of the electrode equals to the rate of cathodic reaction. The curve with potential negative than E_{corr} indicates that the alloy is cathode (be protected), and the curve with potential positive than E_{corr} indicates that the alloy is anode (be corroded). The slope of cathodic line of the alloy was Tafel slope (β_c), which equals to $\Delta E / \Delta \log i$, where E is potential, and i is current density. The corrosion current density (i_{corr}) of each curve was calculated by the intersection of the free corrosion potential and the cathodic Tafel line. Both of the corrosion potential (E_{corr}) and corrosion current density (i_{corr}) of $Cr_{19}Fe_{22}Co_{21}Ni_{25}Mo_{13}$ alloy in these two solutions increased with increasing test temperature. The important data of the curves are listed in Table 2. The potentiodynamic polarization curves of $Cr_{19}Fe_{22}Co_{21}Ni_{25}Mo_{13}$ alloy in HNO_3 solution did not have passivation potential, which meant that this alloy could easily enter the passivation region. The minimum current densities of $Cr_{19}Fe_{22}Co_{21}Ni_{25}Mo_{13}$ alloy in passivation regions (i_{pass}) were about 24 $\mu A/cm^2$, but i_{pass} increased with increasing testing temperatures after higher applied potential (>0.4 V vs. SSE) in HNO_3 solution, shown in Figure 2a. The passivation regions of the alloy under these four testing temperatures all entered breakdown because of the oxygen evolution reaction [14]. The breakdown potential (E_b) were about 0.95 V vs. SSE. The $Cr_{19}Fe_{22}Co_{21}Ni_{25}Mo_{13}$ alloy had similar tendency, which

was tested in deaerated 1M HCl solution, as shown in Figure 2b. However, the corrosion potentials of $Cr_{19}Fe_{22}Co_{21}Ni_{25}Mo_{13}$ alloy were more negative, and corrosion current densities of $Cr_{19}Fe_{22}Co_{21}Ni_{25}Mo_{13}$ alloy were larger in deaerated 1M HCl solution compared with the data tested in deaerated 1M HNO_3 solution. In addition, smaller anodic peaks were observed in the potentiodynamic polarization curves of $Cr_{19}Fe_{22}Co_{21}Ni_{25}Mo_{13}$ alloy in deaerated 1M HCl solution. The passivation potentials (E_{pp}) and anodic critical current densities (i_{crit}) of these curves are listed in Table 2. The current densities of $Cr_{19}Fe_{22}Co_{21}Ni_{25}Mo_{13}$ alloy in passivation regions also increased with increasing testing temperatures in HCl solution after larger applied potential (>0.2 V vs. SSE), shown in Figure 2b. The passivation regions of the alloy under these four testing temperatures were all in breakdown because of the oxygen evolution reaction. The breakdown potentials (E_b) slightly decreased with increasing testing temperature.
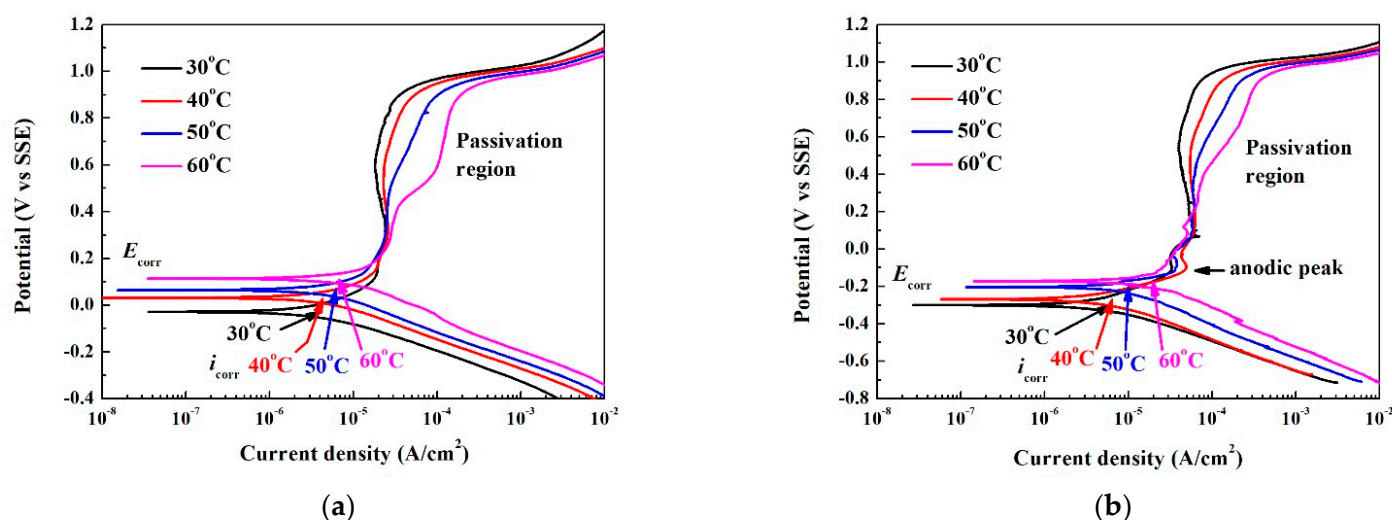

Figure 2. Potentiodynamic polarization curves of $Cr_{19}Fe_{22}Co_{21}Ni_{25}Mo_{13}$ alloy tested in the deaerated solutions of: (**a**) 1M HNO_3 solution and (**b**) 1M HCl solution under different temperatures.

Table 2. Corrosion potentials and corrosion current densities of $Cr_{19}Fe_{22}Co_{21}Ni_{25}Mo_{13}$ alloy tested under different temperatures.

Solution	Items	30 °C	40 °C	50 °C	60 °C
1M HNO$_3$ solution	E_{corr} (V vs SSE)	−0.029	0.031	0.064	0.113
	i_{corr} (µA/cm^2)	4.00	4.30	5.10	7.30
	i_{pass} (µA/cm^2)	23.8	23.7	23.1	24.6
	E_b (V vs. SSE)	0.951	0.951	0.951	0.949
1M HCl solution	E_{corr} (V vs SSE)	−0.30	−0.267	−0.203	−0.172
	i_{corr} (µA/cm^2)	6.00	6.30	9.80	20.0
	E_{pp} (V vs. SSE)	−0.099	−0.091	−0.081	0.080
	I_{crit} (µA/cm^2)	33.0	47.3	38.2	50.6
	i_{pass} (µA/cm^2)	41.0	53.0	58.0	48.6
	E_b (V vs. SSE)	0.971	0.968	0.961	0.951

Figure 3a,b show the comparison of $Cr_{19}Fe_{22}Co_{21}Ni_{25}Mo_{13}$ alloy and commercial 304 stainless steel tested in deaerated 1M HNO_3 and HCl solutions at 30 °C, respectively. Both of the figures show that the corrosion potentials (E_{corr}) of $Cr_{19}Fe_{22}Co_{21}Ni_{25}Mo_{13}$ alloy were more positive than that of 304 stainless steel, and the corrosion current densities (i_{corr}) of $Cr_{19}Fe_{22}Co_{21}Ni_{25}Mo_{13}$ alloy were less than that of 304 stainless steel. The 304 stainless steel had larger anodic peaks compared with $Cr_{19}Fe_{22}Co_{21}Ni_{25}Mo_{13}$ alloy in these two solutions. The current density of passivation region of $Cr_{19}Fe_{22}Co_{21}Ni_{25}Mo_{13}$ alloy

were also less than that of 304 stainless steel. These indicated that the corrosion resistance of $Cr_{19}Fe_{22}Co_{21}Ni_{25}Mo_{13}$ alloy was better than that of 304 stainless steel in these two solutions, especially in the deaerated 1M HCl solution. The corrosion potentials (E_{corr}) and corrosion current densities (i_{corr}) of $Cr_{19}Fe_{22}Co_{21}Ni_{25}Mo_{13}$ alloy and 304 stainless steel are listed in Table 3. Molybdenum could improve the localized corrosion resistance [15,16], especially the attack from the chloride ions. The $Cr_{19}Fe_{22}Co_{21}Ni_{25}Mo_{13}$ alloy thus had a good corrosion resistance in 1M HCl solution.
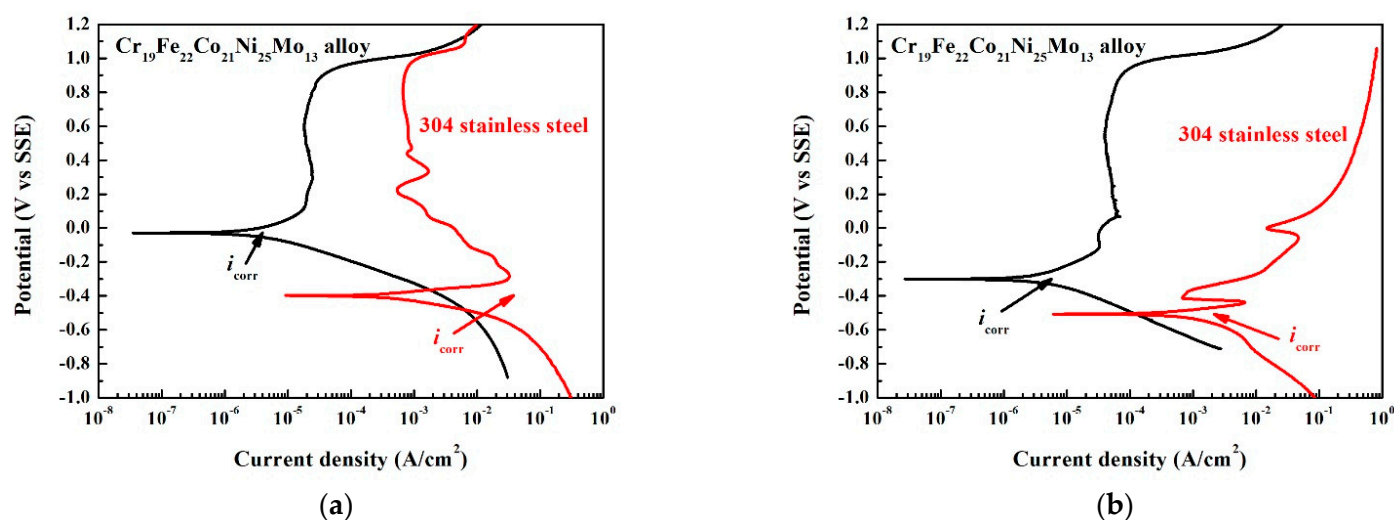

Figure 3. Polarization curves of $Cr_{19}Fe_{22}Co_{21}Ni_{25}Mo_{13}$ alloy and 304 stainless steel tested in the deaerated solutions of: (**a**) 1M HNO_3 solution and (**b**) 1M HCl solution at 30 °C.

Table 3. Corrosion potentials and corrosion current densities of $Cr_{19}Fe_{22}Co_{21}Ni_{25}Mo_{13}$ alloy and 304 stainless steel tested at 30 °C.

Alloy	1M HNO_3 Solution		1M HCl Solution	
	E_{corr} (V vs SSE)	i_{corr} (A/cm^2)	E_{corr} (V vs SSE)	i_{corr} (A/cm^2)
$Cr_{19}Fe_{22}Co_{21}Ni_{25}Mo_{13}$	−0.029	4.0×10^{-6}	−0.300	6.0×10^{-6}
304 stainless steel	−0.399	3.9×10^{-2}	−0.507	2.0×10^{-3}

Figure 4a,b show the morphologies of $Cr_{19}Fe_{22}Co_{21}Ni_{25}Mo_{13}$ alloy after polarization test in the deaerated 1M HNO_3 and HCl solutions, respectively. The corrosion time of each specimen was 1500 s because anodic range was from open circuit potential (OCP) to OCP+1.5V, and the scanning rate was 1 mV/s. These two figures indicates that the corrosion type of $Cr_{19}Fe_{22}Co_{21}Ni_{25}Mo_{13}$ alloy in these two solution were a uniform corrosion. The FCC phase of $Cr_{19}Fe_{22}Co_{21}Ni_{25}Mo_{13}$ alloy was concave in these two figures, which meant that the FCC phase was more severely corroded than the SC phase in $Cr_{19}Fe_{22}Co_{21}Ni_{25}Mo_{13}$ alloy. The standard electrode potentials ($E°$ vs. SSE) of Cr, Fe, Co, Ni, and Mo are −0.962, −0.662, −0.449, −0.472, and −0.422 V, respectively [17]. Molybdenum has the highest standard electrode potential among these elements. The SC phase had higher Mo content, listed in Table 1 and thus had more positive corrosion potential by comparing with the corrosion potential of FCC phase in $Cr_{19}Fe_{22}Co_{21}Ni_{25}Mo_{13}$ alloy. Therefore, the FCC phase was severely corroded and formed a concave morphology.

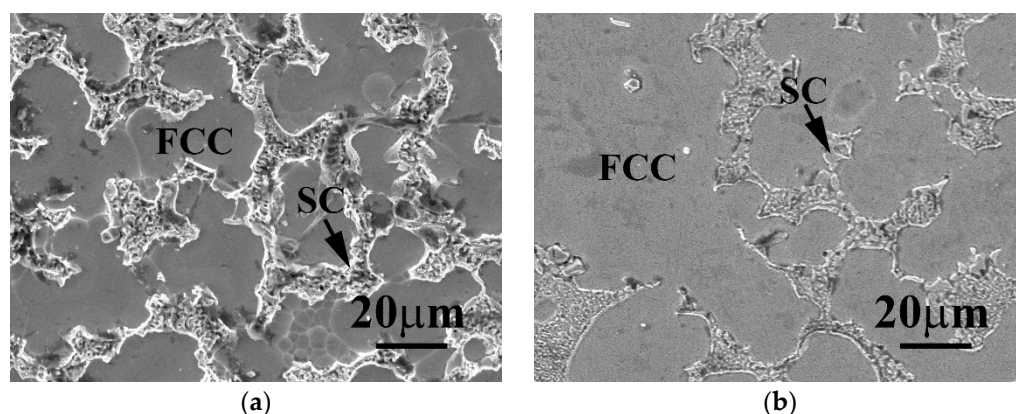**Figure 4.** The micrographs of $Cr_{19}Fe_{22}Co_{21}Ni_{25}Mo_{13}$ alloy after polarization tested in the deaerated solutions of: (**a**) 1M HNO_3 solution and (**b**) 1M HCl solution at 30 °C. The corrosion time of each specimen was 1500 s.

4. Conclusions

The as-cast $Cr_{19}Fe_{22}Co_{21}Ni_{25}Mo_{13}$ alloy had a dendritic structure. The dendrites were an FCC phase, and the interdendritic regions were a eutectic structure of FCC and SC phases. The SC phase had higher Cr and Mo content but lower Fe, Co and Ni content compared with the FCC phase. Both of the corrosion potential and corrosion current density of $Cr_{19}Fe_{22}Co_{21}Ni_{25}Mo_{13}$ alloy increased with increasing testing temperature in deaerated 1M HNO_3 and 1M HCl solutions. The passivation regions of $Cr_{19}Fe_{22}Co_{21}Ni_{25}Mo_{13}$ alloy tested in these two solutions entered breakdown at applied potential of about 0.95 V vs SSE because of the oxygen evolution reaction. The potentiodynamic polarization curves of $Cr_{19}Fe_{22}Co_{21}Ni_{25}Mo_{13}$ alloy in both of 1M HNO_3 and 1M HCl solutions showed better corrosion resistance by comparing with commercial 304 stainless steel. The morphologies of $Cr_{19}Fe_{22}Co_{21}Ni_{25}Mo_{13}$ alloy after polarization tested in 1M HNO_3 and 1M HCl solutions showed a uniform corrosion type. The SC phase was slightly more corroded than the FCC phase because of the higher Mo content.

Author Contributions: Conceptualization, C.-H.T.; methodology, C.-H.T. and P.-M.C.; formal analysis, C.-H.T. and P.-M.C.; investigation, C.-H.T. and P.-M.C.; data curation, C.-H.T. and P.-M.C.; writing—original draft preparation, C.-H.T.; writing—review and editing, C.-H.T.; supervision, C.-H.T.; All authors have read and agreed to the published version of the manuscript.

Institutional Review Board Statement: Not applicable.

Informed Consent Statement: Not applicable.

Data Availability Statement: Not applicable.

Conflicts of Interest: The funders had no role in the design of the study; in the collection, analyses, or interpretation of data; in the writing of the manuscript, or in the decision to publish the results.

References

1. Muangtong, P.; Rodchanarowan, A.; Chaysuwan, D.; Chanlek, N.; Goodall, R. The corrosion behaviour of CoCrFeNi-x (x = Cu, Al, Sn) high entropy alloy systems in chloride solution. *Corros. Sci.* **2020**, *172*, 108740. [CrossRef]
2. Geantă, V.; Voiculescu, I.; Cotrut, M.C.; Vrânceanu, M.D.; Vasile, I.M.; Rosca, J.C.M. Effect of Al on Corrosion Behavior in 3.5% NaCl Solution of Al_xCoCrFeNi High Entropy Alloys. *Int. J. Eng. Res. Afr.* **2021**, *53*, 20–30. [CrossRef]
3. Wang, W.; Wang, J.; Yi, H.; Qi, W.; Peng, Q. Effect of Molybdenum Additives on Corrosion Behavior of $(CoCrFeNi)_{100-x}Mo_x$ High-Entropy Alloys. *Entropy* **2018**, *20*, 908. [CrossRef] [PubMed]

4.	Huang, K.; Chen, L.; Lin, X.; Huang, H.; Tang, S.; Du, F. Wear and Corrosion Resistance of $Al_{0.5}CoCrCuFeNi$ High-Entropy Alloy Coating Deposited on AZ91D Magnesium Alloy by Laser Cladding. *Entropy* **2018**, *20*, 915. [CrossRef] [PubMed]

5.	Lyu, P.; Chen, Y.; Liu, Z.; Cai, J.; Zhang, C.; Jin, Y.; Guan, Q.; Zhao, N. Surface modification of CrFeCoNiMo high entropy alloy induced by high-current pulsed electron beam. *Appl. Surf. Sci.* **2020**, *504*, 144453. [CrossRef]

6.	Yao, Y.; Jin, Y.; Gao, W.; Liang, X.; Chen, J.; Zhu, S. Corrosion Behavior of $AlFeCrCoNiZr_x$ High-Entropy Alloys in 0.5 M Sulfuric Acid Solution. *Metals* **2021**, *11*, 1471. [CrossRef]

7.	Jalbuena, A.A.; Ury, N.; Bae, J.; Faraj, C.; Hanan, K.; Kasnakjian, S.; Logier, J.K.; Mishra, R.S.; Wang, X.; Earthman, J.C. Corrosion of $Al_{0.1}CoCrFeNi$ High Entropy Alloy in a Molten Eutectic Salt. *J. Electrochem. Soc.* **2019**, *166*, C3488. [CrossRef]

8.	Xu, J.; Wang, S.; Shang, C.; Huang, S.; Wang, Y. Microstructure and Properties of CoCrFeNi(WC) High-Entropy Alloy Coatings Prepared Using Mechanical Alloying and Hot Pressing Sintering. *Coating* **2019**, *9*, 16. [CrossRef]

9.	Tsau, C.H.; Tsai, M.C. The effects of Mo and Nb on the microstructures and properties of CrFeCoNi(Nb,Mo) alloys. *Entropy* **2018**, *20*, 648. [CrossRef] [PubMed]

10.	Tsau, C.H.; Yeh, C.Y.; Tsai, M.C. The Effect of Nb-Content on the Microstructures and Corrosion Properties of $CrFeCoNiNb_x$ High-Entropy Alloys. *Materials* **2019**, *12*, 3716. [CrossRef] [PubMed]

11.	Murty, B.S.; Yeh, J.W.; Ranganathan, S.; Bhattacharjee, P.P. *High-Entropy Alloys*, 2nd ed.; Elsevier Co.: Amsterdam, The Netherlands, 2019; pp. 13–30.

12.	Yeh, J.W. Alloy Design Strategies and Future Trends in High-Entropy Alloys. *JOM* **2013**, *65*, 1759–1771. [CrossRef]

13.	Bard, A.J.; Faulkner, L.R. *Electrochemical Methods: Fundamentals and Applications*, 2nd ed.; John Wiley & Sons: New York, NY, USA, 2000; the table on inside back cover.

14.	Callister, W.D., Jr. *Fundamentals of Materials Science and Engineering: An Integrated Approach*, 2nd ed.; John Wiley & Sons, Inc.: New York, NY, USA, 2005; p. 674.

15.	Hashimoto, K.; Asami, K.; Teramoto, K. An X-ray photo-electron spectroscopic study on the role of molybdenum in increasing the corrosion resistance of ferritic stainless steels in HCl. *Corros. Sci.* **1979**, *19*, 3–14. [CrossRef]

16.	Godlewska, E.; Mitoraj-Królikowska, M.; Czerski, J.; Jawańska, M.; Gein, S.; Hecht, U. Corrosion of Al(Co)CrFeNi High-Entropy Alloys. *Front. Mater.* **2020**, *7*, 335. [CrossRef]

17.	Chawla, S.L. *Materials Selection for Corrosion Control*; ASM International: Materials Park, OH, USA, 1993; p. 18.